

Aircraft Cruise Drag Reduction through Variable Camber using Existing Control Surfaces

Thomas A. Reist,^{*} David Koo,[†] and David W. Zingg[‡]

Institute for Aerospace Studies, University of Toronto, Toronto, Ontario, M3H 5T6, Canada

The ability to morph the shape of an aircraft wing to optimize performance is widely accepted as a path to improved aircraft efficiency. A simpler approach is to change the wing camber using existing control surfaces. In this work, a Reynolds-averaged Navier-Stokes based aerodynamic shape optimization methodology is applied to the design of a business jet with variable camber. Variable camber is achieved using the three existing control surfaces on each wing. Multipoint optimization is performed over a range of cruise operating conditions with and without variable camber. Variable camber is found to yield a reduction in drag of approximately 3-11 counts, or 1-5%, over a range of cruise conditions, with the largest reductions seen at lower lift coefficients. The control surface deflections are used to reduce the wing camber at lower lift cruise conditions, leading to an increase in the aircraft angle of attack across most operating points. The increased angles of attack transfer lift to the fuselage, which enables reductions in induced, wave, and trim drag. This additional drag reduction mechanism has not been identified in previous studies and cannot be seen in optimizations that do not include the fuselage and a trim constraint.

Nomenclature

α	=	Angle of attack
C_D	=	Drag coefficient
C_L	=	Lift coefficient
C_M	=	Pitching moment coefficient
C_p	=	Pressure coefficient
δ	=	Control surface deflection angle
h	=	Altitude
\mathcal{J}	=	Objective function

^{*}Research Associate, tom.reist@utoronto.ca

[†]Specialist, Aero Thermal Fluids, david.koo@prattwhitney.com

[‡]University of Toronto Distinguished Professor in Computational Aerodynamics and Sustainable Aviation, Associate Fellow AIAA, dwz@utias.utoronto.ca.

l_{ref}	=	Reference length
M	=	Mach number
t/c	=	Airfoil thickness-to-chord ratio
W	=	Aircraft weight
\mathcal{W}	=	Objective priority weighting
$x_{\text{tail}}, z_{\text{tail}}$	=	Longitudinal and vertical coordinates of horizontal stabilizer
$x_{\text{CG}}, z_{\text{CG}}$	=	Longitudinal and vertical coordinates of center of gravity
\mathcal{Z}	=	Designer priority weighting function

I. Introduction

In order to survive, the aviation sector must drastically reduce its environmental footprint, in particular its impact on climate change, without a substantial increase in the cost of air travel. Whichever energy source becomes prevalent in the future, it is likely to be more expensive than current jet fuel, at least initially; hence the energy efficiency of aircraft must improve substantially. Consequently, drag reduction technologies are a high priority. A recent ICAO report describes several such technologies suitable for introduction by 2037, including, natural laminar flow, hybrid laminar flow control, riblets, and morphing wings, along with an estimate of their likely benefits, based on input provided by industry [1].

A given aircraft cruises at a range of conditions, depending on the payload, fuel mass, speed, and altitude, which translates into a range of lift coefficients, Mach numbers, and Reynolds numbers. As a single wing geometry cannot be optimal for all conditions encountered, wing morphing enables the wing to deform continuously to its optimal shape depending on the particular conditions. The impact of wing morphing on fleet fuel efficiency will depend on the range of cruise conditions encountered and the frequency with which the aircraft are operated near the extremes of the cruise envelope. Finding a means to deform the wing while maintaining safety and reliability and minimizing weight and cost is a challenge. One way to obtain some of the benefits of morphing with reduced cost, risk, and weight is to use existing high-lift flaps and control surfaces to modify the wing shape in cruise, usually accompanied by a means of sealing the slots [2].

Aerodynamic shape optimization can provide a means to determine the optimum wing shape to minimize drag at each cruise condition. The potential benefits of variable geometry can be assessed on this basis and weighed against the cost, risk, and additional weight. Moreover, the nature of the geometric changes can be limited in various ways to make the task of morphing the wing easier, and the impact of such constraints on the drag reduction potential can be evaluated. In addition to reducing drag by varying the wing geometry, wing weight can also be reduced through load alleviation, active flutter suppression, and consideration of static aeroelastic effects.

Early work on variable camber wings includes that of Szodruch and Holbig [3] and Gref [4]. A summary of

developments in adaptive wing technology prior to 2001 is provided by Stanewsky [5]. Examples of investigations of adaptive airfoils are given in Trenker [6], Namgoong et al. [7], Patzold et al. [8], and Zingg et al. [9]. Subsequent work studied the potential of variable geometry wings. For example, Lyu and Martins [10] used aerodynamic shape optimization of a wing with an adaptive morphing trailing edge wing to demonstrate that drag reductions of 1% can be achieved at on-design conditions near cruise, and up to 5% at off-design conditions such as climb, with a fuel burn reduction for a representative mission of 1%. Variable camber was controlled by 80 design variables which could alter the camber over the aft 45% of the chord. Curiale and Zingg [11] compared five distinct types of morphing through aerodynamic shape optimization of a regional-class aircraft wing, considering only aerodynamic effects, and showed cruise drag reductions on the order of 2% for a fully adaptable wing and 1% if the morphing is restricted to the trailing edge region. Wakayama and White [12] and Stanford [13] included aerostructural effects and showed that significant weight savings and hence fuel burn reductions can be achieved through load alleviation, efficient span loads, and active flutter suppression. Ting et al. [14] and Rodriguez et al. [15, 16] also considered aeroelastic effects in their studies of the variable camber continuous trailing edge flap system. Burdette and Martins [17] performed both aerodynamic and aerostructural optimization of trailing edge morphing on the Common Research Model wing-body-tail configuration. Morphing was accomplished by 32 morphing variables over the aft 10% of the chord. The morphing wing was optimized over 240 flight conditions, with the wing shape held fixed, and the morphing shapes at each operating point determined by the optimizer. They found that, within the portion of the envelope that the aircraft would typically encounter, the drag savings were approximately 1%. Near the edge of the envelope, e.g. high C_L -Mach combinations, the savings were up to 5%. At these extreme conditions, they illustrate the drag reduction comes from reduced shock strength and closer to elliptical loading. Using the optimized results, they also performed mission analysis and computed fuel burn reductions of 2.7% for a representative long-range mission, including aerodynamic and aeroelastic effects.

In the papers referred to above, the primary mechanisms by which variable camber reduces drag, which are most significant at conditions other than cruise, e.g. climb, are twofold: 1) spanwise lift distribution tailoring for induced drag reduction, and 2) wave drag reduction through camber modification. In this paper, we describe an additional drag reduction mechanism that can be effective at cruise conditions where the wing camber is reduced at lower lift coefficients, enabling an increase in the aircraft angle of attack and therefore fuselage lift. This in turn reduces the wing loading, with benefits in induced and wave drag, and reduces trim drag as well. This drag reduction mechanism is not seen in morphing wing studies that consider a wing alone. Moreover, past studies that consider full aircraft have emphasized spanwise lift distribution tailoring and wave drag reduction and have not observed, or at least described, the additional important drag reduction mechanism shown in the present work.

The objectives of this paper are twofold: 1) to investigate the cruise drag reduction potential of variable camber wings for a small business jet, where the variable camber is achieved via existing control surfaces, which are sealed for this purpose, as on the Airbus A350XWB [18], and 2) to demonstrate an additional mechanism by which variable

camber wings reduce drag at cruise conditions by allowing the aircraft to operate at an optimal angle of attack across more operating conditions, which reduces wing loading and hence induced, wave, and trim drag.

II. Methodology

A. Multipoint Optimization Problem Formulation

Variable camber is studied through multipoint optimization in order to account for the variations in altitude, speed, and load seen by a typical small business aircraft during cruise over a range of missions. Each combination of speed, weight, and altitude produces conditions that can be expressed in terms of a lift coefficient, Mach number, and Reynolds number that uniquely determine the drag coefficient. In this work, variations in Reynolds number are ignored and only variations in lift and Mach number are considered. The multipoint objective function, \mathcal{J} , is the priority-weighted sum of the drag coefficient at each operating point:

$$\mathcal{J} = \sum_{j=1}^{N_{\text{opt}}} \mathcal{W}_j C_{D_j}, \quad (1)$$

with the priority weights, \mathcal{W}_j , being chosen by the designer to account for expected operations.

An alternative multipoint formulation is presented by Buckley and Zingg [19] in which the weights for the various operating conditions in the composite objective function are determined to approximate the following integral using a quadrature rule

$$\int_{h_1}^{h_2} \int_{W_1}^{W_2} \int_{M_1}^{M_2} C_D(M, w, h) \mathcal{Z}(M, W, h) dM dW dh \quad (2)$$

where the range of altitudes is given by $[h_1, h_2]$, the range of aircraft weights by $[W_1, W_2]$, and the range of Mach numbers by $[M_1, M_2]$. The priority weighting function $\mathcal{Z}(M, W, h)$ can be taken as unity or as a function that reflects the frequency with which the aircraft is expected to fly at particular conditions in the cruise flight envelope. Although this is a rigorous approach that enables minimization of cruise fuel burn over an aircraft fleet based on expected operations, our approach here is to use a multipoint objective function as in Equation 1 with five operating conditions in order to reduce the computational expense of the optimization.

B. Aerodynamic Shape Optimization Methodology

The aerodynamic shape optimization is performed using the Jetstream software suite, which is built up from four main components: a flow and adjoint solver for the Reynolds-Averaged Navier-Stokes equations[20, 21], an integrated geometry parameterization and mesh deformation scheme[22], a free-form and axial deformation geometry control interface, and the gradient-based nonlinear optimization package SNOPT[23].

Jetstream's parallel flow solver makes use of second-order summation-by-parts operators for spatial discretization, combined with simultaneous approximation terms to enforce boundary and interface conditions[24]. The discrete governing equations are solved implicitly using an inexact Newton method, while the linear solver uses the Generalized Minimum Residual (GMRES) method combined with approximate Schur preconditioning. Turbulence is incorporated using the Spalart-Allmaras one-equation model, including the SA-neg and QCR modifications, which is fully coupled with the rest of the flow equations. The flow is evaluated on multi-block structured grids, and the solver has demonstrated scalability up to thousands of processors. The flow solver has been verified through participation in the AIAA's Fifth Drag Prediction Workshop [20, 25] which showed good agreement between this solver and other established solvers using the same turbulence model for predicting full-configuration aircraft performance at transonic conditions. Moreover, the Spalart-Allmaras turbulence model has been extensively validated for attached and mildly separated transonic aerodynamic flows.

During optimization, the computational mesh is fitted to a B-spline control volume, creating an analytical approximation to the initial geometry. Jetstream deforms the analytical geometry representation by displacing the B-spline control points on the aerodynamic surface. A finite-element linear elasticity model is then used to propagate displacements on the surface to the volume mesh. The resulting method is robust, computationally inexpensive, and allows for significant shape changes while maintaining grid quality.

Free-Form Deformation (FFD) volumes are used to provide the optimizer with a means to control the B-spline parameterization representing the surface of the geometry, which is embedded inside the FFD volume[26]. The optimizer is free to manipulate the control points defining the FFD volume, which results in a change to the aerodynamic surface within. Each FFD volume can also be associated with an axial curve, allowing control of the wing span, sweep, and dihedral angle. The axial curve is a non-uniform rational B-spline curve, allowing the designer freedom to create winglets, nonlinear sweep, and closed wing geometries.

At each iteration of the optimization, the flow solution is computed around the latest geometry, which is then followed by the solution of the corresponding flow adjoint problem. The discrete adjoint problem is solved using GCROT(m,k)[27], a flexible and simplified version of the GCROT method[28, 29]. The flow adjoint solution is then used to find the solution of the mesh adjoint problem, which incorporates terms that arise from the analytical mapping of the mesh to the B-spline control surface. The resulting gradient is provided to SNOPT (Sparse Nonlinear OPTimizer) [23], a sparse SQP method. After SNOPT updates the design variables, the B-spline control volume is deformed and the computational mesh is updated, leading to the next iteration. SNOPT takes into account user-defined linear constraints, which are used for simple geometric relationships, as well as nonlinear constraints such as lift and moment forces. The latter category of constraints require additional adjoint solutions.

This aerodynamic shape optimization suite has been validated through participation in the AIAA's Aerodynamic Design Optimization Discussion Group [30, 31] as well as through cross-validation with an industrial aerodynamic

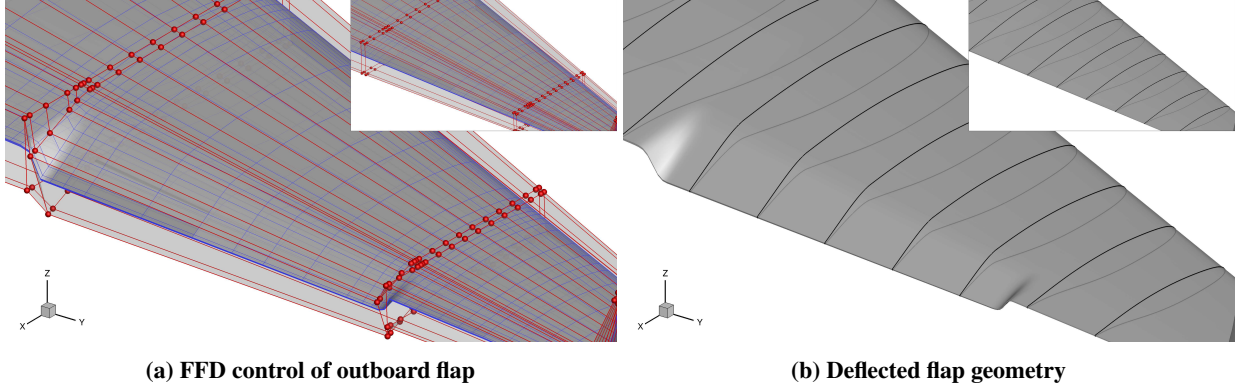


Fig. 1 The FFD parameterization and the resulting geometry of a deflected control surface.

shape optimization code with application to turbulent, transonic aircraft configurations[32].

C. Control Surface Modelling

Variable camber is achieved using trailing edge control surfaces. The control surfaces are deflected using the FFD control net described above. The FFD points over the aft portion of the chord that enclose the control surface are rotated as a group by the deflection angle about the hinge line. This in turn deforms the underlying B-spline parameterization and hence surface CFD grid. This process is illustrated in Figure 1. To create a more defined bend near the hinge line and at the ends of the control surface, the FFD control points are concentrated around the control surface edges in both the chordwise and spanwise direction. Figure 1 shows that this approach, combined with the analytical B-spline surface methodology, can maintain smooth transitions even with relatively large flap deflections. This approach maintains a sealed slot and maintains a continuous and smooth surface, and as such does not capture any discontinuities that may arise at the control surface edges in an actual implementation. Reist et al.[32] validated this methodology on a NACA 66(216)-216 airfoil with a sealed flap and showed good agreement with experimental results.

III. Optimization Problem

A. Objective Function

The flight conditions, given in Table 1, are typical of a business jet, centered around flight at $M = 0.80$ and $C_L = 0.45$. The Reynolds number based on mean aerodynamic chord of 13.6 million is kept fixed for all flight conditions, as the effect of the changes in Reynolds number is considerably smaller than the effects of the variation in lift coefficient and Mach number. The objective is to optimize the aircraft using section shape, twist, angle of attack, and variable camber (if applicable) design variables, to minimize a composite objective function based on the drag coefficient at the six cruise operating conditions. The objective function is of the form given in Equation 1, with the priority weights, \mathcal{W}_j , given in Table 1.

Table 1 Operating points for variable camber optimization

Operating point	Mach number	Lift coefficient	Priority weight
1	0.80	0.40	2.0
2	0.80	0.45	4.0
3	0.80	0.50	2.0
4	0.83	0.30	1.0
5	0.83	0.35	2.0
6	0.83	0.40	1.0

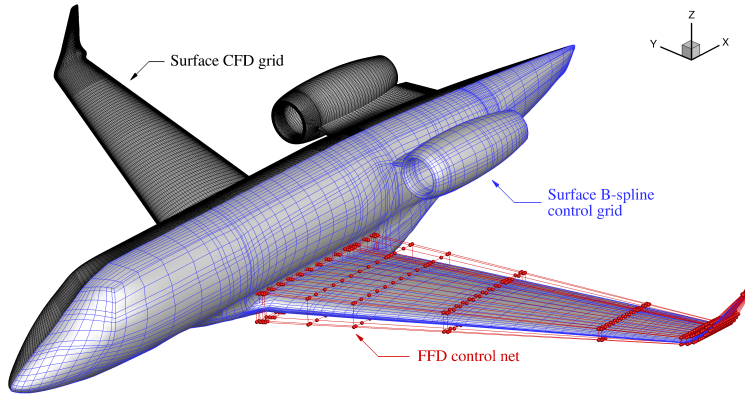


Fig. 2 Isometric view of the initial geometry, a small business jet.

Two optimizations are conducted. The first, called the baseline, is formulated as a conventional multipoint problem, with the goal of creating a single geometry that can only change angle of attack to meet each flight condition - i.e. no variable camber is used. The performance of this design provides a baseline with which to compare the performance of the variable camber design. In the variable camber formulation, the optimizer is given the additional freedom to vary the three control surface angles at each of the six flight conditions. The optimized wings cannot be considered as real aircraft wing designs, given that numerous considerations in the aerodynamic design of a wing have been neglected, such as buffet and low-speed operation, not to mention static and dynamic aerostructural considerations. Therefore, the main focus is on the relative performance between the two wings, as opposed to their absolute performance. Moreover, we do not attempt to determine the cruise fuel burn benefit over a specific mission or range of missions, as this will be dependent on the particular missions chosen. Rather, we will concentrate on the relative performance at the six operating conditions considered in the composite objective function, which provides a clear picture of the benefits of the variable-camber approach.

The starting geometry is the wing-body-nacelle-pylon configuration shown in Figure 2, which is representative of a small business jet aircraft. Both the nacelle and pylon are mounted with zero angle of incidence relative to the fuselage. The incident angles are kept constant during the optimization, but the lift produced by these surfaces will vary with the angle of attack for the entire configuration.

The aircraft geometry does not include a horizontal stabilizer, so trim is accounted for through a penalty term on lift that accounts for the lift on the tail required to maintain trim. The lift coefficient that must satisfy the specified operating conditions in Table 1 is given by:

$$C_{L_{\text{trim}}} = C_{L_{\text{tail-off}}} + C_{M_{\text{tail-off}}} \frac{l_{\text{ref}}}{\cos(\alpha)(x_{\text{tail}} - x_{\text{CG}}) + \sin(\alpha)(z_{\text{tail}} - z_{\text{CG}})}. \quad (3)$$

where l_{ref} is the reference length taken to be the mean aerodynamic chord (MAC), $(x_{\text{tail}} - x_{\text{CG}})$ and $(z_{\text{tail}} - z_{\text{CG}})$ are the streamwise and vertical distances between the tail's MAC quarter chord and the center of gravity (CG). In this work, a T-tail is used, with the distances set accordingly. The CG location and horizontal tail MAC quarter chord are indicated in Figure 3. Any reference to the lift coefficient in the remainder of the paper refers to the trimmed lift coefficient, i.e. $C_L = C_{L_{\text{trim}}}$.

Increased negative lift on the tail will increase total drag through the associated increase in $C_{L_{\text{trim}}}$, as well as through an induced drag penalty term computed from the tail lift. This induced tail drag is calculated analytically and assumes a tail aspect ratio of 4.6 and span efficiency factor of 0.9. The results obtained are not sensitive to the tail aspect ratio and span efficiency assumptions, as the explicit tail trim drag is small. Although the present approach may not produce the correct spanwise load distribution on the wing, it is expected to be sufficient for the purposes of this paper, which are to estimate the drag reduction benefit of variable camber and to understand the mechanism by which it is achieved. Moreover, a T-tail is assumed, so the interaction between the wing and the tail is reduced relative to a low tail.

The optimization is performed on a 13 million node, 519 block mesh, while final drag values are computed using Richardson extrapolation on successively refined grids with 24 million and 51 million nodes.

B. Design Variables and Constraints

Figure 3 shows the location of each design section, which corresponds to the location of an FFD control slice, as well as the variable camber control surfaces. There are six design sections on the main wing and an additional seven sections at the winglet. At each design section, the twist (about the leading edge) and eighteen FFD points on each of the upper and lower surfaces for local section shape control serve as design variables. The clustered design sections at the blended winglet are required for the FFD volume to properly resolve the wing's curvature. On the clustered design sections at the winglet root, the FFD section shape variables are all free, while the twist of the intermediate sections is interpolated to prevent infeasible geometries. When the results are presented in Section IV, no variables are at their bounds unless otherwise stated.

Variable camber is achieved using three control surfaces: an inboard flap, an outboard flap, and an aileron, covering the aft 25% of the chord. These control surfaces are illustrated in Figure 3. The deflection angle of each control surface for each operating point makes up the variable camber design variables. There are therefore 18 deflection design

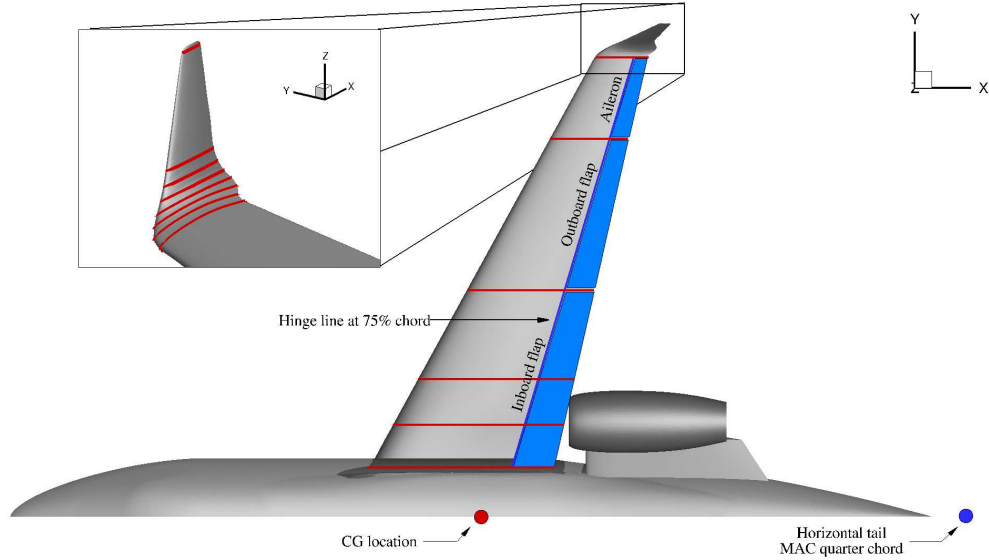


Fig. 3 Design section locations (red lines), along with variable camber control surfaces (blue)

variables, each of which is limited to $\pm 3^\circ$. These deflection variables are only active in the variable camber cases.

At every flight condition, the angle of attack, α , is bounded to be within $\pm 3^\circ$ in order to maintain a comfortable deck angle. The following geometric constraints are applied in order to mimic real-world design restrictions:

- The maximum t/c at each design section is greater than or equal to that of the initial geometry
- The t/c at 15% and 90% chord at each design station is greater than or equal to that of the initial geometry
- The leading edge radius at each design station is greater than or equal to that of the initial geometry
- The twist on the 2nd and 3rd design sections (those on the interior of the inboard flap) is interpolated between the 1st and 4th design stations in order to preserve a relatively straight hinge line
- To prevent excessive geometric changes to the fuselage and belly fairing, at the root design section the twist variable is limited to $\pm 4^\circ$ and the FFD control points controlling the section shape are limited to move by a maximum of $\pm 10\%$ of their initial location

The baseline optimization has 516 design degrees of freedom (the number of design variables is greater than this, as some design variables are linearly related to each other.) In the variable camber formulation, the additional freedom to vary the three control surface angles at each of the six flight conditions yields a total of 534 design degrees of freedom.

IV. Results

The convergence histories of the optimizations, including normalized optimality and feasibility measures are plotted in Figure 4, showing that both optimizations are well converged. Each function evaluation takes approximately one hour with each operating point being analyzed in parallel on 519 processors each. The relative merit functions in Figures 4a and 4b are normalized by the same value, and show that the increased freedom of variable camber allows for a greater

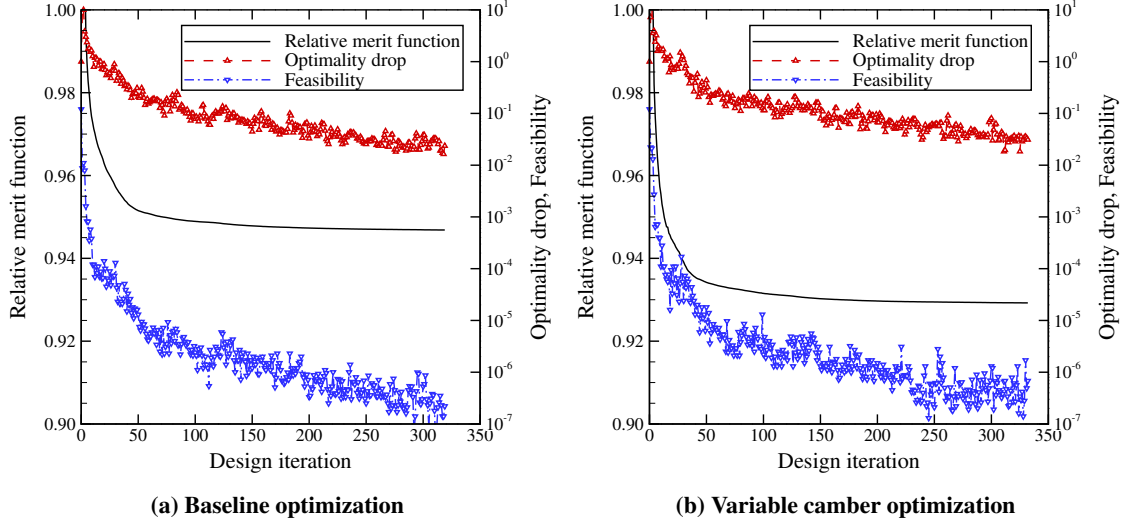


Fig. 4 Plots of merit function, optimality, and feasibility showing optimization convergence.

Table 2 Comparison of baseline and variable camber optimized configurations. The drag coefficient, C_D , is computed via Richardson extrapolation, and is shown in drag counts.

M	C_L	Baseline		Variable camber			
		α [°]	C_D	α [°]	C_D	ΔC_D	ΔC_D [%]
0.80	0.40	2.33	235.9	3.00	230.8	-5.1	-2.2
0.80	0.45	2.67	253.9	3.00	250.2	-3.7	-1.5
0.80	0.50	3.00	280.3	3.00	274.4	-5.9	-2.1
0.83	0.30	1.55	216.3	2.61	205.1	-11.2	-5.2
0.83	0.35	1.86	233.7	2.70	225.4	-8.3	-3.6
0.83	0.40	2.17	255.2	2.83	252.4	-2.8	-1.1

reduction in the objective. At the converged solution, no design variables are at their bounds except for some shape variables at the wing-fuselage junction and some angles of attack - as will be discussed below. The thickness constraints including t/c , maximum t/c , and leading edge radius constraints are active at the majority of the design stations.

Table 2 summarizes the results of both optimizations, giving drag coefficient values, the angle of attack, and the drag reductions resulting from the variable camber for each operating condition. Drag values are computed via Richardson extrapolation from a grid convergence study on grids with up to 51 million nodes. The grid convergence plot is shown in Figure 5 for the optimized baseline design. The horizontal dashed lines indicate the Richardson extrapolated values. The plot for the variable camber design is similar. Variable camber allows for between a 2.8 and 11.2 drag count, or 1-5%, reduction depending on the operating condition. The control surface deflections and angles of attack for each operating point are shown in Figure 6. As in previous wing-body optimizations done by Jetstream [33], the optimizer tends toward flying at the maximum angle of attack permitted. In the baseline design, it can only design for a 3° angle of attack at the maximum lift flight condition, $M = 0.80$ and $C_L = 0.50$, while all other conditions are at a lower angle

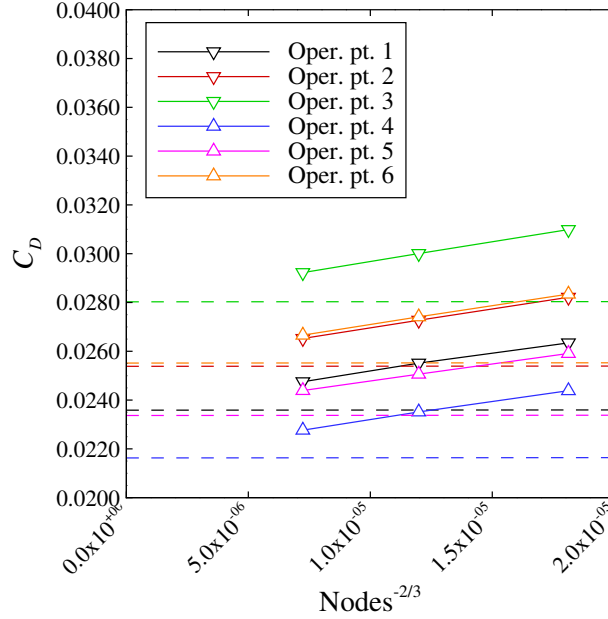


Fig. 5 Sample grid convergence plot for the optimized baseline.

of attack. The additional freedom of variable camber allows the aircraft to fly at an angle of attack of 3° for the three $M = 0.80$ conditions, and 2.6° - 2.8° for the $M = 0.83$ conditions. The drag benefit of the variable camber wing is greatest at the flight conditions where it can fly at a much higher angle of attack than the baseline design. The flap and aileron deflections are optimized to decrease the wing camber as the lift requirement decreases between operating points, which allows for the aircraft to operate at a higher angle of attack across more operating points, thus producing induced, wave, and trim drag benefits as will be discussed below. Note that it is the relative deflection angle between operating points for a given control surface that is important, as the optimizer can trade-off changes in twist, camber, and control surface deflection to achieve the optimal angle of attack at each operating point.

Figure 7a shows the change in lift produced by the wing, fuselage-nacelle-pylon, and tail* at each operating point due to variable camber. In the baseline design, the share of lift produced by the fuselage and nacelle-pylon stays roughly constant at around 12%, since only the angle of attack can vary at each flight condition. For the variable camber design, at each operating point the increased angle of attack together with modified wing camber increases the lift carried by the fuselage and nacelle-pylon. This results in two benefits: 1) Decreased load carried by the wing. Decreasing the load on the wing reduces induced drag and, at some operating points, wave drag, as will be discussed later. In addition, the wing's center of pressure acts aft of the center of gravity, so reduced wing loading leads to a weaker nose-down moment which must be compensated for by the tail - thus reducing trim drag. 2) The fuselage and nacelle-pylon both have a positive $\frac{\partial C_M}{\partial \alpha}$, so allowing them to operate at a higher angle of attack leads to a smaller nose-down pitching moment that must be trimmed out, again leading to a reduction in trim drag. The reduced tail load resulting from these mechanisms

*Recall that the tail is not explicitly modelled. The tail lift refers to the lift needed by the tail to maintain trim, which can be found from Equation 3.

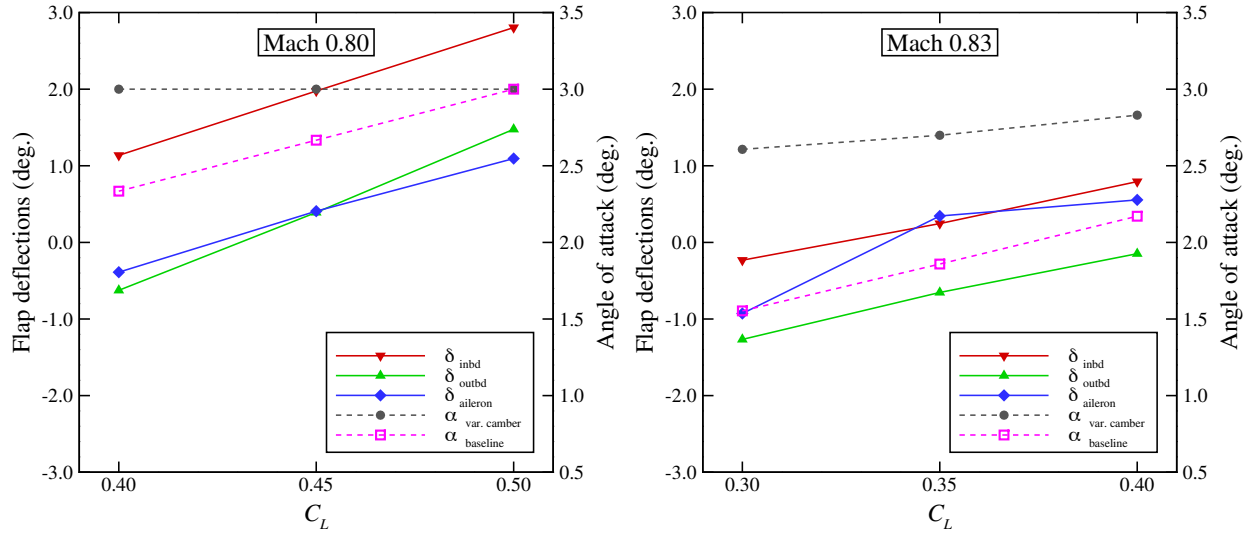


Fig. 6 Control surface deflections for the variable camber design and angles of attack for both designs. Positive δ means flap down, increasing camber.

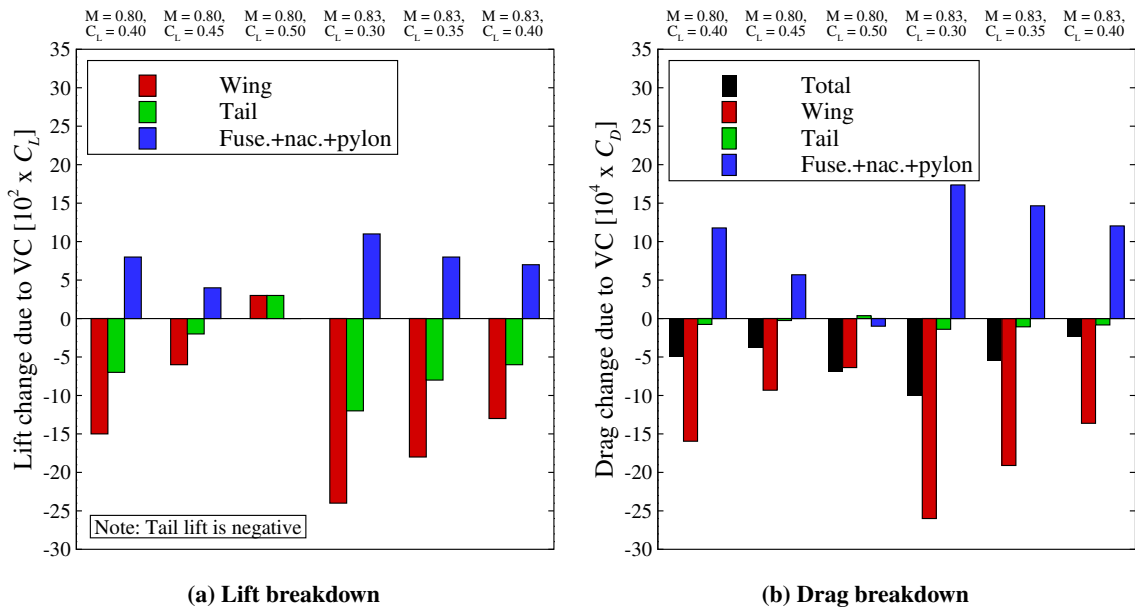


Fig. 7 Changes in lift and drag on each aircraft component enabled by variable camber.

is evident in Figure 7a. The use of variable camber yields the highest fraction of fuselage and nacelle-pylon lift and the lowest tail load at the $M = 0.83$ and $C_L = 0.30$ operating point, which, from Table 2, exhibits the greatest performance benefit. These mechanisms for reducing drag via variable camber require that the whole aircraft be included in the optimization of the variable camber wing.

The following breakdowns expand on the drag reduction mechanisms discussed above. The vast majority of the drag reduction is due to reduced pressure drag, which includes induced, wave, and form drag. Friction drag changes by only 0.3 drag counts on average. This is not unexpected as there is little change in surface area, and the only other friction

drag reduction mechanism would be through increased laminar flow. Fully turbulent flow is assumed and, although a small amount of laminar flow can exist, its extent is not affected by the variable camber. There is also little change in form drag, and no separation is seen in any of these cases. Therefore, the drag reduction can come from lower induced and wave drag. This decomposition between these two sources is further broken down as follows.

A breakdown of drag based on aircraft component is shown in Figure 7b. Note that these breakdowns are computed on the optimization level grid, so the absolute magnitudes differ slightly from those in Table 2. For each operating point, the wing produces less drag when variable camber is used, while the fuselage/nacelle/pylon produce more (with the exception of the main operating point at $M = 0.80$, $C_L = 0.50$). This reflects the lift breakdown in Figure 7a. The tail drag is also reduced at all operating points except the main design point due to the reduction in tail lift. The drag reductions on the fuselage/nacelle/pylon and tail are due to reduced loading. The drag reduction on the wing is due to induced and/or wave drag reductions. Illustrations of the shock surfaces are shown in Figure 8 for both the baseline and variable camber designs across all operating points. These suggest that for the first three operating points at Mach 0.80 variable camber offers a reduction in wave drag, while for the last three operating points at Mach 0.83, wave drag increases. However, the last three operating points are at conditions for which variable camber offers some of the largest benefits. Hence, the benefit at these operating points is coming from lower induced drag stemming from the reduced wing loading. Lower induced drag would also be enabled by more optimal spanwise load distributions. However, the induced drag is less sensitive to changes in the spanwise load distribution than to changes in lift coefficient. The spanwise load distributions found by the optimizer will be aerodynamically optimal as modelled, and the absence of an explicitly included tail in the CFD model has an impact on the optimal load distribution. To determine the optimal spanwise load distributions in addition to the variable camber benefit, the tail should be included in the CFD model. However, the use of a T-tail somewhat diminishes this dependence.

Figure 9 shows the optimized airfoil shapes and pressure distributions for the baseline and variable camber designs. Slices are shown at 6 stations along the wing which correspond to the $1/3$ and $2/3$ span location on each control surface. This data is extracted from flow solutions computed on the optimization-level grid. The starting geometry (not shown) for the optimizations exhibited a strong shock over most of the span. This has been significantly weakened in both optimizations, and in some cases more so through variable camber, for example on the inboard sections illustrated in Figure 9 and Figure 8b. Note that the section shapes are not very different between the baseline and variable camber designs. In Figure 10, the airfoil shapes and pressure distributions are shown for the fourth flight condition at $M = 0.83$, $C_L = 0.30$, where the variable camber offers the greatest benefit over the baseline design. The control surface deflections are more visible here, as the variable camber wing is noticeably less cambered toward the trailing edge at each section. As shown in Figure 8d, the shock strengths are not reduced through variable camber at this operating point.

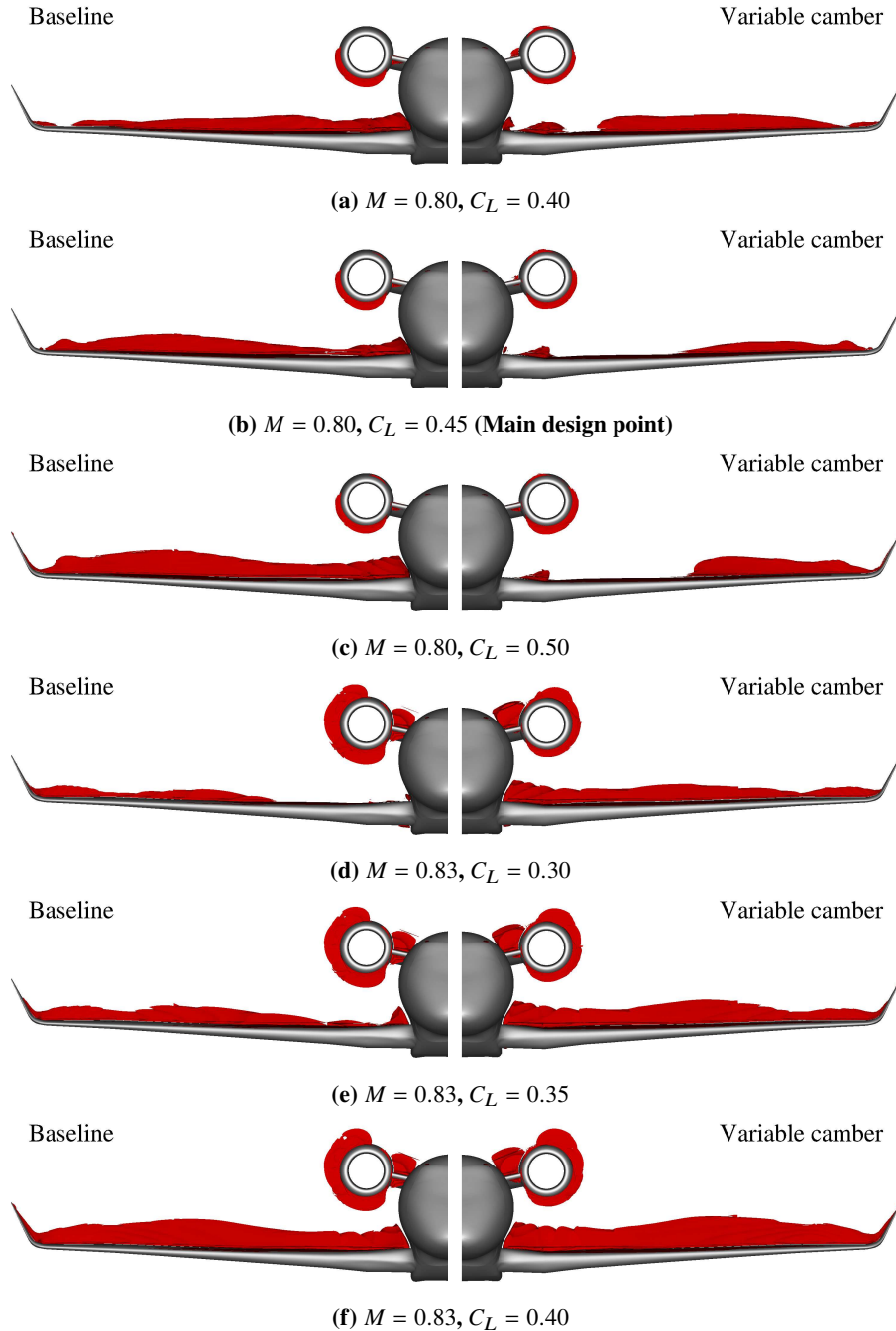


Fig. 8 Shock surfaces on the optimized baseline and variable camber designs.

A. Variable Camber as a Retrofit

To investigate the potential of using variable camber as a retrofit technology, i.e. using control surfaces to change the camber without redesigning the whole wing, the baseline optimized design is reoptimized using variable camber and angle of attack design variables only. The wing shape is held fixed as that from the baseline optimization. Table 3 shows the percentage of the full variable camber drag benefit that is achieved when variable camber is used as a retrofit. Even

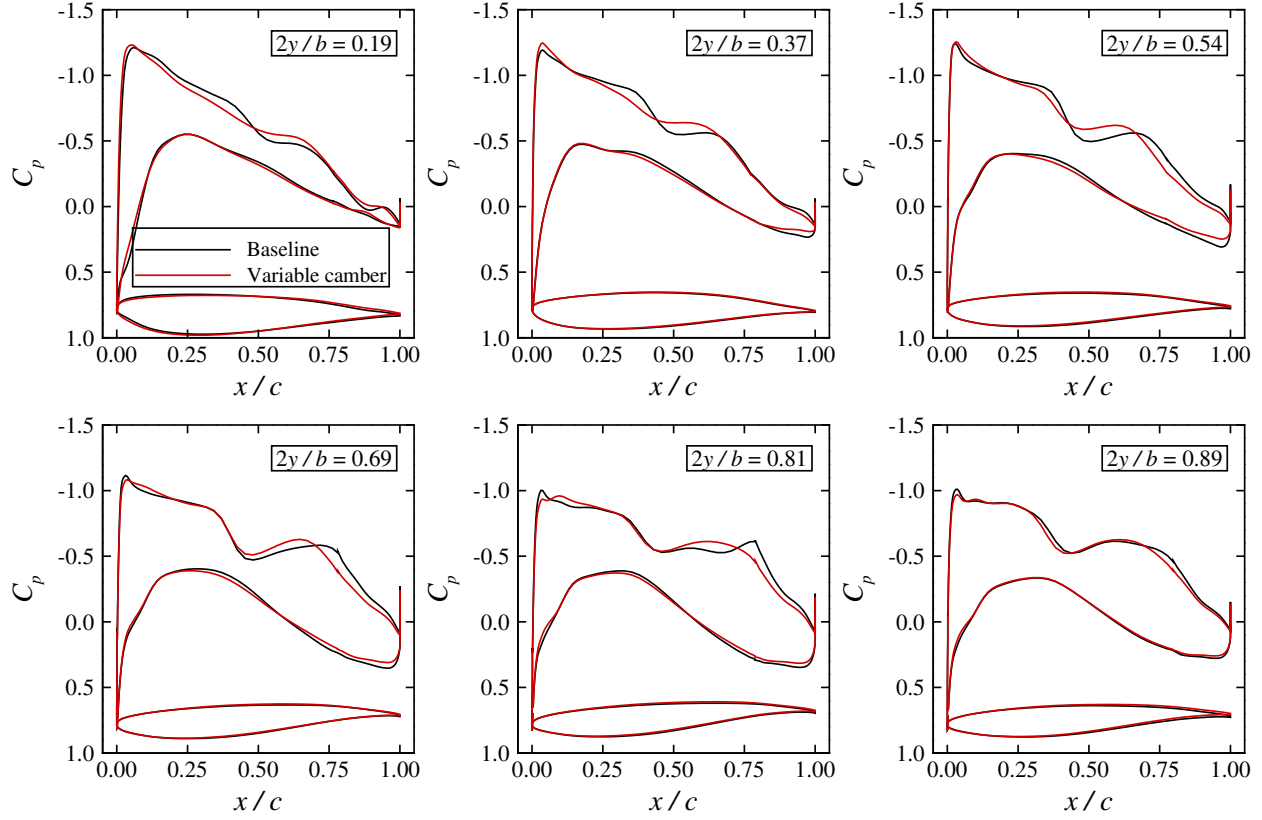


Fig. 9 Section C_p and airfoil shapes for $M = 0.80$, $C_L = 0.45$, the design operating point.

Table 3 Percentage of the variable camber drag reduction achieved using retrofit variable camber.

M	C_L	Retrofit benefit
0.80	0.40	35.9%
0.80	0.45	1.5%
0.80	0.50	30.9%
0.83	0.30	69.6%
0.83	0.35	46.9%
0.83	0.40	25.1%

with the fixed geometry, variable camber produces on average 35% of the benefit obtained when the variable camber deflections and geometry are optimized simultaneously. With the addition of the deflection variables, the optimizer increases the angle of attack and de-cambers the wing using the control surfaces, as shown in Figure 11, for all operating points except for operating point three, the highest lift point. The baseline optimized design operates at 3° for this operating point, which decreases to 2.71° when variable camber is introduced.

Figure 12 shows the pressure distributions for the baseline, variable camber, and retrofit variable camber designs for the fourth operating point; the operating point for which variable camber is the most beneficial. Due to the similar shapes produced by the baseline and variable camber optimizations as mentioned previously, the retrofit variable camber case

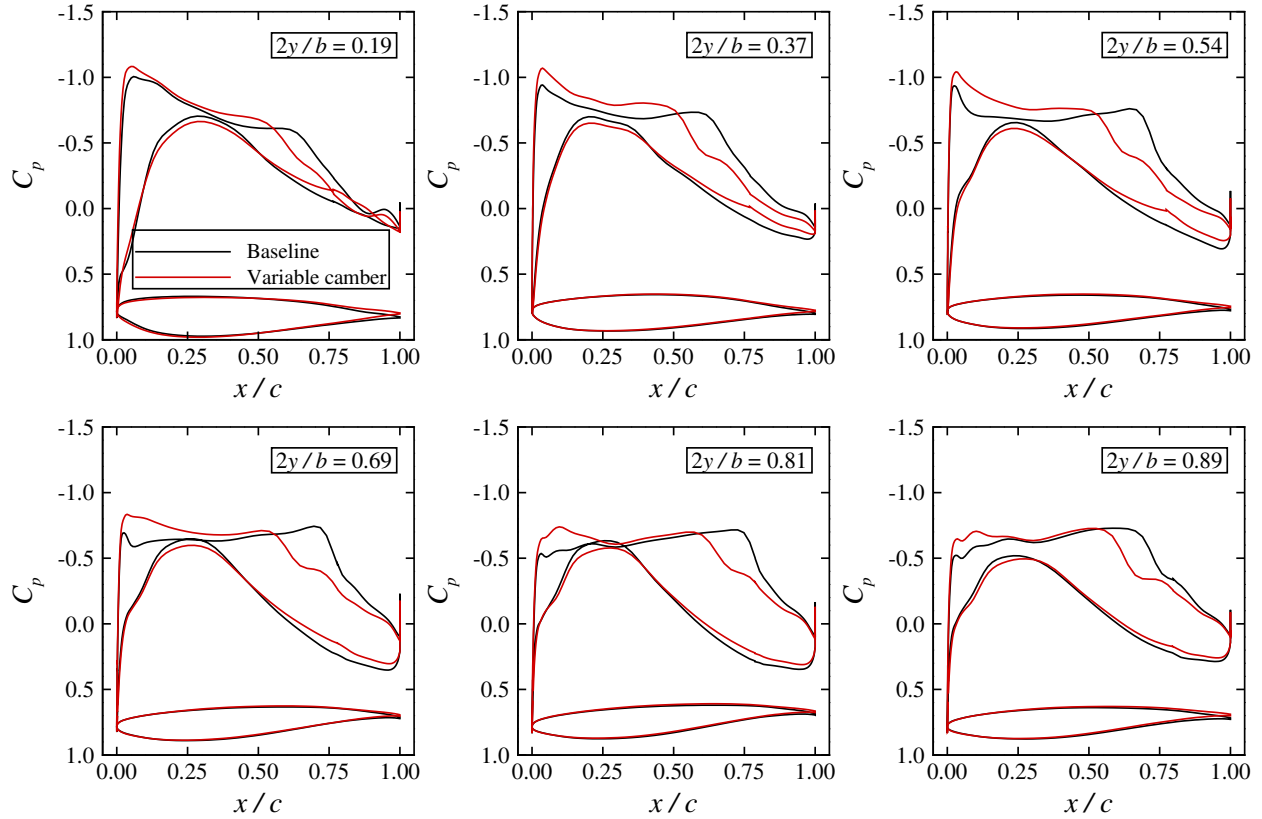


Fig. 10 Section C_p and airfoil shapes for $M = 0.83$, $C_L = 0.30$, the flight condition with the greatest ΔC_D and deflections.

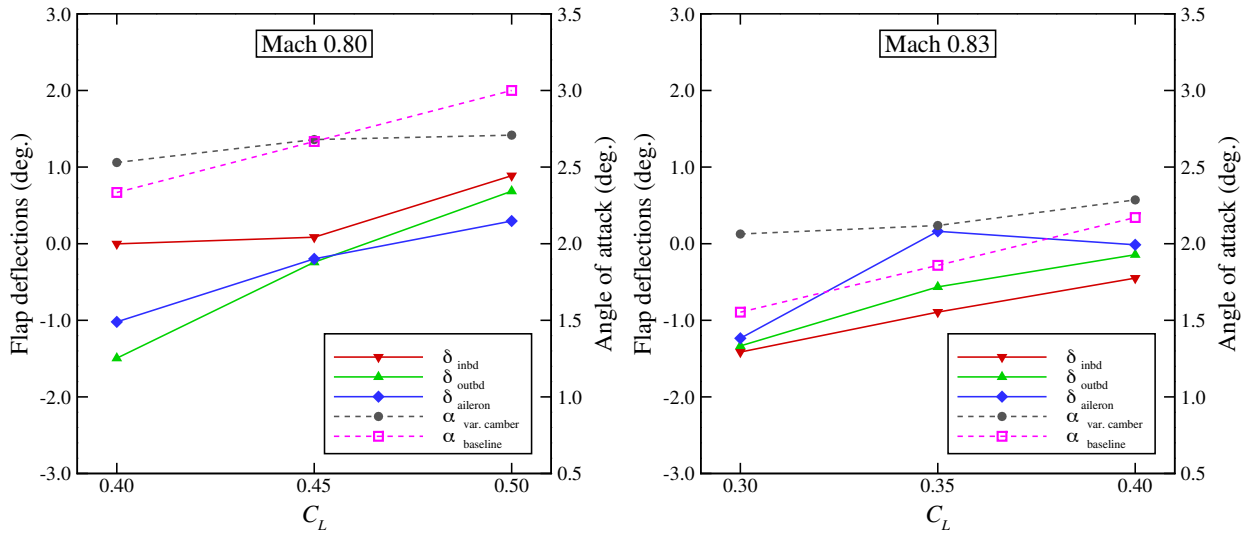


Fig. 11 Control surface deflections for the variable camber retrofit design and angles of attack for both designs. Positive δ means flap down, increasing camber.

is able to achieve very similar pressure distributions to the full variable camber case through control surface deflections and changes in angle of attack.

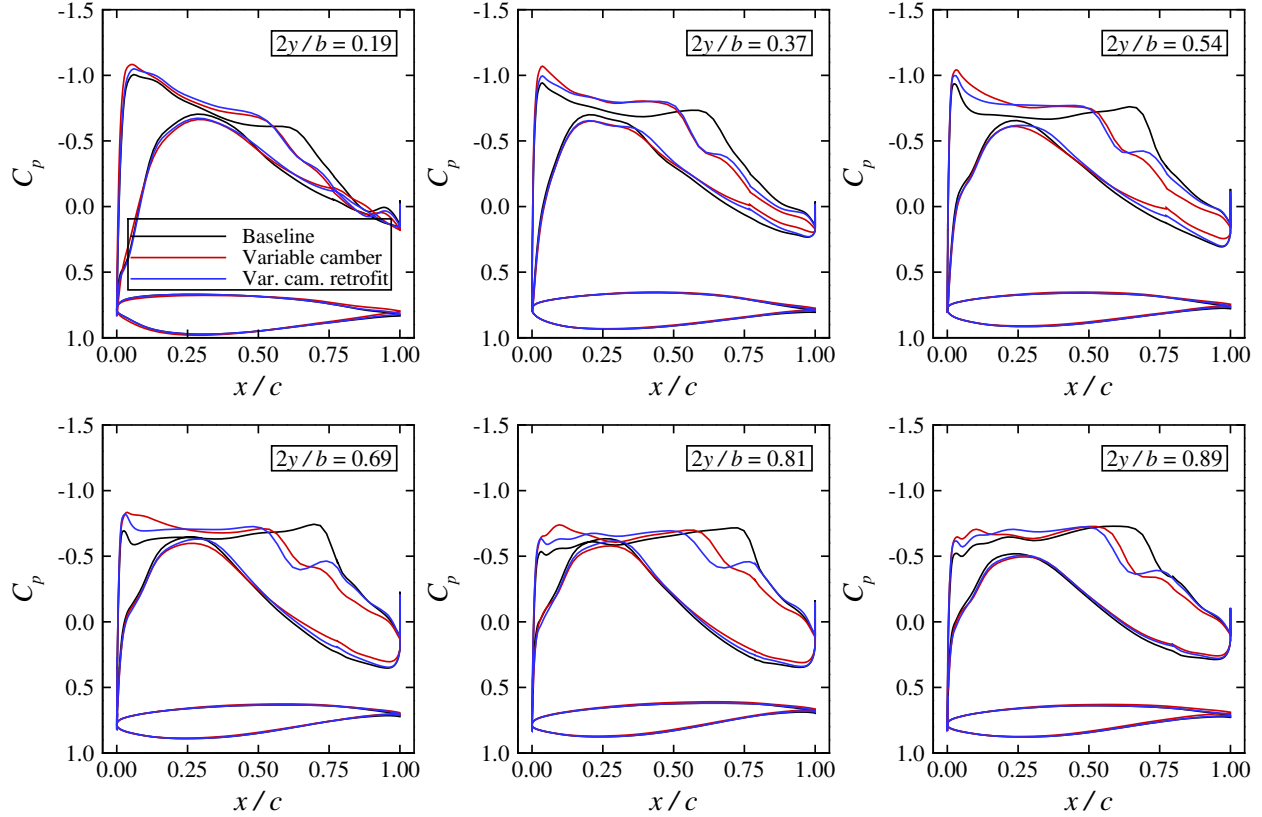


Fig. 12 Comparison of the C_p and airfoil shapes for the fourth operating point, including the variable camber retrofit design.

This result demonstrates the potential of using existing control surfaces to change the wing camber and achieve performance benefits. In the retrofit case as with the full variable camber case, the control surfaces modelled here use sealed gaps and produce a continuous outer mould line. If control surfaces that did not produce a continuous mould line were to be used, the implications of any gaps and steps would need to be assessed.

V. Conclusions

A high-fidelity aerodynamic shape optimization methodology was applied to a variable camber wing for a business jet. Using three control surfaces, the optimizer was able to reduce drag by 1-5% across a range of cruise flight conditions. The optimizer utilizes the flaps and ailerons to alter the camber to maintain a relatively high aircraft angle of attack at low lift coefficient flight conditions. In doing so, it alters the lift distribution such that a greater share of the lift is produced by the fuselage, nacelle, and pylon, thereby reducing the load on the wing, leading to reductions in induced, wave, and trim drag. It also takes advantage of the pitching characteristics of the fuselage to minimize trim drag. This mechanism is also beneficial if variable camber is used as a retrofit technology. When variable camber is used on a fixed wing that was not optimized for variable camber, the benefit is on average about 35% of that obtained with the wing and

deflections optimized simultaneously.

The results here suggest that modelling the interaction between the wing, fuselage, and other lifting surfaces is crucial to designing variable camber and morphing wings. This gives the optimizer the freedom to distribute lift efficiently among the various aircraft components and achieve drag reductions beyond those that would be seen in a wing-only optimization. In particular, this drag reduction mechanism is important at cruise conditions, whereas the conventionally accepted mechanisms of wave drag reduction and spanwise lift distribution tailoring are likely to be more effective at the extremes of the operating envelope.

Future work could include additional operating points to cover off-design conditions and the inclusion of the tail in the CFD model. Another potential benefit of variable camber is in load alleviation. Future studies which account for aeroelastic effects so as to assess the benefit of using existing control surfaces for load alleviation should be considered.

Acknowledgements

The authors gratefully acknowledge the financial support provided by the National Sciences and Engineering Research Council of Canada. Computations were performed on the Niagara supercomputer at the SciNet HPC Consortium. SciNet is funded by: the Canada Foundation for Innovation under the auspices of Compute Canada, the Government of Ontario, Ontario Research Fund - Research Excellence, and the University of Toronto.

References

- [1] Cumpsty, N., Mavris, D., Alonso, J., Catalano, F., Evers, C., Goutines, M., Gronstedt, T., Hileman, J., Joselzon, A., Khaletskii, I., Ogilvie, F., Ralph, M., Sabnis, J., Wahls, R., and Zingg, D. W., “Independent Expert Integrated Technology Goals Assessment and Review for Aircraft and Engines,” *ICAO Doc 10127*, Montreal, Canada, 2019.
- [2] Sutcliffe, M., Reckzeh, D., and Fischer, M., “HICON Aerodynamics – High Lift Aerodynamics Design for the Future,” *25th Congress of the International Council of the Aeronautical Sciences*, Hamburg, Germany, 2005.
- [3] Szodruch, J. and Hilbig, R., “Variable Wing Camber for Transport Aircraft,” *Progress in Aerospace Sciences*, Vol. 25, No. 3, 1988, pp. 287–328. doi:[https://doi.org/10.1016/0376-0421\(88\)90003-6](https://doi.org/10.1016/0376-0421(88)90003-6).
- [4] Gref, E., “The Development and Design Integration of a Variable Camber Wing for Long/Medium Range Aircraft,” *The Aeronautical Journal*, Vol. 94, No. 939, 1990, pp. 301–312. doi:<https://doi.org/10.1017/S0001924000023186>.
- [5] Stanewsky, E., “Adaptive Wing and Flow Control Technology,” *Progress in Aerospace Sciences*, Vol. 37, No. 7, 2001, pp. 583–667. doi:[https://doi.org/10.1016/S0376-0421\(01\)00017-3](https://doi.org/10.1016/S0376-0421(01)00017-3).
- [6] Trenker, M., “Design Concepts for Adaptive Airfoils with Dynamic Transonic Flow Control,” *Journal of Aircraft*, Vol. 40, No. 4, 2003, pp. 734–740. doi:<https://doi.org/10.2514/2.3152>.
- [7] Namgoong, H., Crossley, W. A., and Lyrantzis, A. S., “Aerodynamic Optimization of a Morphing Airfoil Using Energy as an Objective,” *AIAA Journal*, Vol. 45, No. 9, September 2007. doi:<https://doi.org/10.2514/1.24355>.
- [8] Patzold, M., Lutz, T., Kramer, E., and Wagner, S., “Numerical Optimization of Finite Shock Control Bumps,” *AIAA Aerospace Sciences Meeting and Exhibit*, AIAA-2006-1054, Reno, Nevada, January 2006. doi:<https://doi.org/10.2514/6.2006-1054>.
- [9] Zingg, D. W., Diosady, L., and Billing, L., “Adaptive Airfoils for Drag Reduction at Transonic Speeds,” *24th AIAA Applied Aerodynamics Conference*, AIAA-2006-3656, San Francisco, CA, June 2006. doi:<https://doi.org/10.2514/6.2006-3656>.
- [10] Lyu, Z. and Martins, J. R. R. A., “Aerodynamic Shape Optimization of an Adaptive Morphing Trailing-Edge Wing,” *Journal of Aircraft*, Vol. 52, No. 6, 2015. doi:<https://doi.org/10.2514/1.C033116>.
- [11] Curiale, N. J. and Zingg, D. W., “Morphing Wings: A Study Using Aerodynamic Shape Optimization,” *AIAA Scitech 2018*, AIAA-2018-1910, Kissimmee, Florida, January 2018. doi:<https://doi.org/10.2514/6.2018-1910>.
- [12] Wakayama, S. and White, E. V., “Evaluation of Adaptive Compliant Trailing Edge Technology,” *33rd AIAA Applied Aerodynamics Conference*, AIAA-2015-3289, Dallas, Texas, June 2015. doi:<https://doi.org/10.2514/6.2015-3289>.
- [13] Stanford, B. K., “Static and Dynamic Aeroelastic Tailoring with Variable- Camber Control,” *Journal of Guidance, Control, and Dynamics*, Vol. 39, No. 11, 2016, pp. 2522–2534. doi:<https://doi.org/10.2514/1.G000413>.
- [14] Ting, E., Chapparo, D., Nguyen, N., and Fujiwara, G. E. C., “Optimization of Variable-Camber Continuous Trailing-Edge Flap Configuration for Drag Reduction,” *Journal of Aircraft*, Vol. 55, No. 6, 2018. doi:<https://doi.org/10.2514/1.C034810>.

- [15] Rodriguez, D. L., Aftosmis, M. J., Nemec, M., and Anderson, G. R., "Optimization of Flexible Wings with Distributed Flaps at Off-design Conditions," *Journal of Aircraft*, Vol. 53, No. 6, 2016. doi:<https://doi.org/10.2514/1.C033535>.
- [16] Rodriguez, D. L., Aftosmis, M. J., Nemec, M., and Anderson, G. R., "Distributed-Flap Layout Trade Study on a Highly Flexible Common Research Model," *2018 Multidisciplinary Analysis and Optimization Conference*, AIAA-2018-3639, Atlanta, Georgia, June 2018. doi:<https://doi.org/10.2514/6.2018-3639>.
- [17] Burdette, D. A. and Martins, J. R. R. A., "Impact of Morphing Trailing Edges on Mission Performance for the Common Research Model," *Journal of Aircraft*, Vol. 56, No. 1, 2019. doi:<https://doi.org/10.2514/1.C034967>.
- [18] Reckzeh, D., "Multifunctional Wing Moveables: Design of the A350XWB and the Way to Future Concepts," *29th Congress of the International Council of the Aeronautical Sciences*, St. Petersburg, Russia, 2014.
- [19] Buckley, H. P. and Zingg, D. W., "An Approach to Aerodynamic Design through Numerical Optimization," *AIAA Journal*, Vol. 51, No. 8, August 2013. doi:<https://doi.org/10.2514/1.J052268>.
- [20] Osusky, M. and Zingg, D. W., "A Parallel Newton-Krylov-Schur Flow Solver for the Reynolds-averaged Navier-Stokes Equations Discretized using Summation-by-Parts Operators," *AIAA Journal*, Vol. 51, No. 12, December 2013, pp. 2833–2851. doi:<https://doi.org/10.2514/1.J052487>.
- [21] Osusky, L., Buckley, H. P., Reist, T. A., and Zingg, D. W., "Drag Minimization based on the Navier-Stokes Equations Using a Newton-Krylov Approach," *AIAA Journal*, Vol. 53, No. 6, June 2015, pp. 1555–1577. doi:<https://doi.org/10.2514/1.J053457>.
- [22] Hicken, J. E. and Zingg, D. W., "Aerodynamic Optimization with Integrated Geometry Parameterization and Mesh Movement," *AIAA Journal*, Vol. 48, No. 2, February 2010, pp. 401–413. doi:<https://doi.org/10.2514/1.44033>.
- [23] Gill, P., Murray, W., and Saunders, M. A., "SNOPT: An SQP Algorithm for Large-Scale Constrained Optimization," *SIAM Review*, Vol. 47, No. 1, 2005, pp. 99–131. doi:<https://doi.org/10.1137/S0036144504446096>.
- [24] Del Rey Fernández, D. C., Hicken, J. E., and Zingg, D. W., "Review of Summation-By-Parts Operators with Simultaneous Approximation Terms for the Numerical Solution of Partial Differential Equations," *Computers and Fluids*, Vol. 95, 2014, pp. 171–196. doi:<https://doi.org/10.1016/j.compfluid.2014.02.016>.
- [25] Osusky, M., Boom, P., and Zingg, D. W., "Results from the Fifth AIAA Drag Prediction Workshop Obtained with a Parallel Newton-Krylov-Schur Flow Solver Discretized using Summation-by-Parts Operators," *31st AIAA Applied Aerodynamics Conference*, AIAA-2013-2511, San Diego, CA, June 2013. doi:<https://doi.org/10.2514/6.2013-2511>.
- [26] Gagnon, H. and Zingg, D., "Two-level Free-Form and Axial Deformation for Exploratory Aerodynamic Shape Optimization," *AIAA Journal*, Vol. 53, No. 7, July 2015, pp. 2015–2026. doi:<https://doi.org/10.2514/1.J053575>.
- [27] Hicken, J. E. and Zingg, D. W., "A Simplified and Flexible Variant of GCROT for Solving Nonsymmetric Linear Systems," *SIAM Journal on Scientific Computing*, Vol. 32, No. 3, June 2010, pp. 1672–1694. doi:<https://doi.org/10.1137/090754674>.

- [28] de Sturler, E., “Nested Krylov methods based on GCR,” *Journal of Computational and Applied Mathematics*, Vol. 67, No. 1, 1996, pp. 15–41. doi:[https://doi.org/10.1016/0377-0427\(94\)00123-5](https://doi.org/10.1016/0377-0427(94)00123-5).
- [29] Hochschule, T., Zurigo, P., Scientifico, C., Di, C., and de Sturler, E., “Truncation Strategies for Optimal Krylov Subspace Methods,” *SIAM Journal on Numerical Analysis*, Vol. 36, No. 3, 5 1999, pp. 864–889. doi:<https://doi.org/10.1137/S0036142997315950>.
- [30] Telidetzki, K., Osusky, L., and Zingg, D. W., “Application of Jetstream to a Suite of Aerodynamic Shape Optimization Problems,” *52nd Aerospace Sciences Meeting*, AIAA-2014-0571, National Harbor, MD, January 2014. doi:<https://doi.org/10.2514/6.2014-0571>.
- [31] Lee, C., Koo, D., Telidetzki, K., Buckley, H., Gagnon, H., and Zingg, D. W., “Aerodynamic Shape Optimization of Benchmark Problems Using Jetstream,” *53rd AIAA Aerospace Sciences Meeting*, AIAA-2015-0262, Kissimmee, FL, January 2015. doi:<https://doi.org/10.2514/6.2015-0262>.
- [32] Reist, T. A., Zingg, D. W., Rakowitz, M., Potter, G., and Bannerjee, S., “Multi-Fidelity Optimization of Hybrid Wing-Body Aircraft with Stability and Control Requirements,” *Journal of Aircraft*, Vol. 56, No. 2, 2019, pp. 442–456. doi:<https://doi.org/10.2514/1.C034703>.
- [33] Reist, T. A., Koo, D., Zingg, D. W., Bochud, P., Castonguay, P., and Leblond, D., “Cross-Validation of High-Fidelity Aerodynamic Shape Optimization Methodologies for Aircraft Wing-Body Optimization,” *AIAA Journal*, Vol. 58, No. 6, February 2020. doi:<https://doi.org/10.2514/1.J059091>.